RESEARCH ARTICLE | JULY 31 2023

Analysis of the wake flow behind concave curved cylinders with velocity measurements by particle image velocimetry and modal decomposition FREE

Matteo Chiatto ; Caroline Cardinale ; Jessica K. Shang ; Francesco Grasso

Physics of Fluids 35, 075153 (2023)
https://doi.org/10.1063/5.0158000

Physics of Fluids ARTICLE pubs.aip.org/aip/pof

Analysis of the wake flow behind concave curved cylinders with velocity measurements by particle image velocimetry and modal decomposition

Cite as: Phys. Fluids **35**, 075153 (2023); doi: 10.1063/5.0158000
Submitted: 13 May 2023 · Accepted: 11 July 2023 ·
Published Online: 31 July 2023

Matteo Chiatto,[1,a)] Caroline Cardinale,[2] Jessica K. Shang,[3] and Francesco Grasso[4,5]

AFFILIATIONS

[1]Department of Industrial Engineering, University of Naples "Federico II," Naples 80125, Italy
[2]Department of Mechanical and Civil Engineering, Caltech, Pasadena, California 91125, USA
[3]Department of Mechanical Engineering and Laboratory for Laser Energetics, University of Rochester, Rochester, New York 14623, USA
[4]Department of Mechanical and Aerospace Engineering, Princeton University, Princeton, New Jersey 08544, USA
[5]DynFluid Laboratory, CNAM-Arts et Métiers Paris Tech, Paris 75013, France

[a)]**Author to whom correspondence should be addressed:** matteo.chiatto@unina.it

ABSTRACT

The properties of the wake flow behind concave curved cylinders have been investigated analyzing simultaneously the mean velocity profiles extracted along concentric arcs parallel to the cylinder axis and the dynamically most relevant coherent structures obtained by spectral proper orthogonal decomposition. These analyzes have allowed us to determine the position, the extension, and the evolution of the different wake regimes. The velocity measurements have been obtained through the stereo particle image velocimetry (stereo-PIV) technique. The study considers various Reynolds numbers, based on cylinder diameter ($240 < Re < 840$), and curvatures. The quarter-of-ring cylinder is first analyzed. Near the cylinder root, the flow exhibits a topology dominated by an oblique vortex shedding, contrary to what is observed in the literature for similar geometric configurations. We attribute this disagreement to differences in the treatment of the free-end conditions that play a role in triggering the shedding regime. We find that the local shedding inclination is driven by the axial velocity, whereas its extension and wavelength depend mainly on the Reynolds number. The near free-end region presents, instead, two counter-rotating standing vortices that induce a cross-wise velocity directed toward the cylinder root and a tip vortex that expands evolving downstream. As the Reynolds number increases, the wake presents irregularities and the shedding spreads becoming nearly normal to the incoming flow. At smaller curvatures, the cylinder free-end becoming more inclined with respect to the incoming flow, and the free-end effects are enhanced. The interaction with the vortex sheets of the standing vortices that develop at the leeward side weakens. As a consequence, these vortices stretch in the stream-wise direction giving rise to the trailing vortices that stem from the cylinder surface and affect the cross-wise velocity distributions.

I. INTRODUCTION

Flows behind curved cylinders exhibit complex wakes with different shedding regimes depending on the curvature, the aspect ratio, and the Reynolds number. These flows are frequently encountered in marine hydrodynamics applications, such as catenary risers that connect seabed pipelines to deep-water floating or fixed offshore platforms. The interest in this topic has greatly increased in the last few years, especially from the numerical point of view. However, the underlying mechanisms of the wake formation and evolution have not been fully analyzed.

Curved cylinders are usually considered in two different configurations, referred to as convex and concave orientation. Being the free-stream in the plane of curvature, a convex configuration experiences the flow toward the outer face of the cylinder, whereas a concave configuration refers to an opposite flow direction. From an experimental point of view, these two configurations correspond to the cylinder free-end pointing, respectively, downstream and upstream. A schematic of the concave configuration is reported in Fig. 1. The left panel shows the cylinder position with respect to the incoming flow, which goes from left to right. The right panel introduces the reference system,

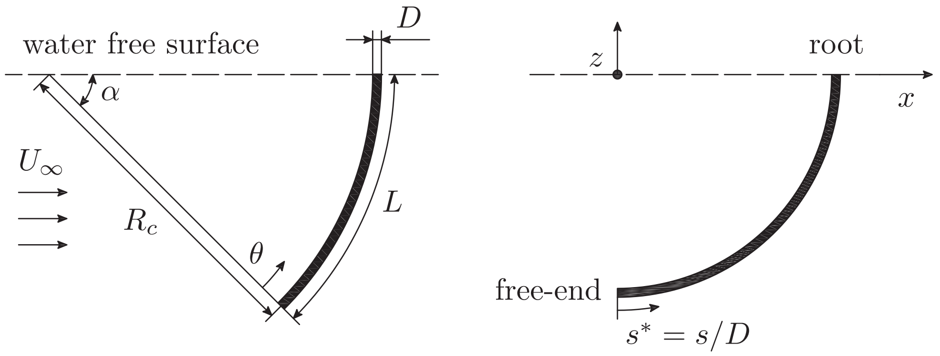

FIG. 1. Outline of curved cylinders in concave configuration with the reference system. The figure illustrates the $\alpha = 45°$ (left panel) and $\alpha = 90°$ (right panel) configurations, respectively.

where x, y, and z represent, respectively, the stream-wise, the span-wise, and the vertical axes. The cylinder's curvature is in the x–z plane. The cylinders have an arc length L, a radius of curvature R_c, and an angle of curvature α. Note that s represents the curvilinear abscissa moving along a concentric arc in the leeward side of the cylinder; it points from the free-end to the root of the cylinder and is made non-dimensional by the cylinder diameter, $s^* = s/D$. In the discussion of the results, we also use the angular position θ along the concentric arc that spans between zero (at the free-end) and α (at the cylinder root). For flows around curved cylinders, the Reynolds number is defined in terms of the cylinder diameter, D, the incoming flow velocity U_∞ (aligned with the stream-wise direction), and the kinematic viscosity ν ($Re = U_\infty D/\nu$).

One of the first investigations of the flow behind a constant curvature cylinder was presented by Miliou *et al.*,[1] at $Re = 100$, and then, it was extended by Miliou *et al.*[2] to the $Re = 500$ case. The configuration used by those authors is a quarter-of-ring ($\alpha = 90°$) that was numerically studied (direct numerical simulation, DNS) in a convex configuration with a horizontal extension ($L_h/D = 10$) at the end of the cylinder and in concave orientation without and with a vertical extension at the root of the cylinder ($L_v/D = 6$). Those authors found that, in a convex configuration, a regular curved vortex shedding at both Reynolds numbers is produced, with only one dominant shedding frequency. The concave configuration, instead, showed vortex shedding limited to the region behind the vertical extension for both Reynolds numbers. No vortex shedding was observed in the absence of the vertical extension; the suppression was attributed to a production of the stream-wise vorticity, which makes the shear layer less susceptible to rolling up. The same configuration was numerically analyzed by de Vecchi *et al.*[3] at $Re = 100$ and later experimentally by Assi *et al.*[4] to $750 \leq Re \leq 15\,000$ also include forced oscillations (translational and rotational). For the base condition, no vortex shedding was observed. A detailed description of the turbulent wake behind a convex curved cylinder was presented by Gallardo *et al.*[5] at $Re = 3900$, considering the same geometry of Miliou *et al.*[2] with both vertical and horizontal extensions. They concluded that the wake can be divided into two main regions: (1) the upper wake (close to the cylinder root) that is characterized by a periodic shedding of primary vortices partially aligned with the cylinder axis and a secondary axial flow next to the lee-side and (2) the lower part that shows a less vigorous vortex shedding with high three-dimensional effects and less-coherent wake structures.

Investigations of the wake flow were experimentally conducted by Shang *et al.*[6] considering finite curved cylinders in both convex and concave configurations at various curvature angles and aspect ratios (L/D), for $234 \leq Re \leq 916$. For convex configurations, the pressure gradient goes from the cylinder root to the free-end, producing an oblique shedding at a constant angle, whereas cylinders in the concave orientation can present different wake regimes depending on Re and L/D: (1) two shedding modes, the normal shedding (with the vortex filament oriented nearly normal to the free-stream) and the oblique shedding with an inclination of the vorticity vector produced by the span-wise velocity component and (2) two non-shedding regimes, the first one appearing close to the free-end, where the wake separates forming two counter-rotating stationary vortices, and the second one occurring when the separated vortices lift off the body and align with the free-stream. In contrast to what was observed by Gallardo *et al.*,[5] those authors concluded that for moderate curvatures and high aspect ratios, the concave cylinders present a wake dominated by oblique and normal shedding. As the curvature increases, they showed that the normal shedding disappears and the non-shedding and oblique shedding regions increase in stream- and cross-wise directions.

High-fidelity numerical simulations were presented by Jiang *et al.*,[7,8] who analyzed the wake behind concave cylinders considering the same geometry studied by Miliou *et al.*,[2] focusing on the effect of straight extensions appended to both cylinder ends at various Reynolds numbers less than 500. For limited vertical extensions ($L_v/D \leq 6$), they retrieved a wake dominate by standing counter-rotating vortices and no vortex shedding. Different shedding regimes were also observed at higher L_v/D. Through the analysis of the axial velocity along concentric arcs from the leeward side of the cylinder, they identified tree different flow regimes: a non-shedding regime behind the surface of the quarter-of-ring, a strongly oblique shedding behind the vertical extension that becomes only slightly oblique close to the end of the extension. They also reported the evolution of the wake for increasing Reynolds numbers, observing the development of three-dimensional structures that were ascribed to both instabilities typical of straight cylinders and usually referred to as type-A and type-B instabilities (which are different instabilities of the primary vortex core, and that appear as secondary wavy structures with different origins and length scales in the span-wise direction[9]) and to the vortex dislocation phenomenon.[10] The analysis was later extended to $Re = 3900$ by Jiang *et al.*,[11] who identified the occurrence of another phenomenon related to the formation of periodic asymmetric helical vortex pair.

More recently, Chiatto *et al.*,[12] using the data of Shang *et al.*,[6] identified the most energetically and dynamically relevant wake flow structures by means of spectral proper orthogonal decomposition (SPOD). Those authors highlighted that, as the Reynolds number increases, the leading shedding frequency experiences a first reduction due to the occurrence of type-A instability, followed by a Strouhal number increase related to a gradual energy transfer between flow structures during the transition from type-A to type-B instabilities. They also showed that vortex dislocation produces a second reduction in the Strouhal number.

From the above discussion, one may conclude the existence of a disagreement between numerical simulations, which show a non-shedding wake, and experimental measurements that exhibit different shedding flow regimes at low *Re*. We argued that this difference is related to the treatment of the free-end conditions. Indeed, as highlighted by Shang *et al.*,[6] at low *Re* curved cylinders behave like straight cylinders, whose wake is strongly affected by the disturbances introduced by the free-end conditions.[13,14]

The three-dimensional structures produced at the cylinder free-end interact with the vortex shedding, modifying the pressure gradient in the direction of the cylinder axis, and affecting the evolution of the entire wake.[15,16] Depending on the Reynolds number, the aspect ratio, and the cylinder inclination angle, a side-tip stream-wise vortex pair may arise at the free-end. These types of structures have been found in straight and inclined circular- and square-section configurations both numerically and experimentally.[17,18] At low aspect ratios, side-tip vortices dominate the entire flow field behind the cylinder, whereas for high aspect ratios, they are limited to the region close to the free-end where they interact with the existing standing vortex pair inducing a further cross-wise velocity.[19]

A summary of the main contributions on the wake flows behind concave curved cylinders, with details on the Reynolds numbers analyzed, the curvatures, and type of investigations, is reported in Table I.

A. Aim of the work

This work is a contribution to the limited experimental literature on the wake behind curved cylinders where the free-stream lies in the plane of curvature. It also aims to clarify the effects of the free-end conditions that are often neglected in most of the numerical investigations, and the analysis is conducted considering Reynolds numbers in the laminar and in the turbulent flow regimes.

TABLE I. Main contributions on the wake flows behind concave curved cylinders.

Reference	*Re*	Geometry	Investigation details
Miliou *et al.*[1]	100	$\alpha = 90°$	DNS
Miliou *et al.*[2]	100 and 500	$\alpha = 90°$ + vertical extension	DNS
de Vecchi *et al.*[3]	100	$\alpha = 90°$	DNS
Shang *et al.*[6]	$234 \leq Re \leq 916$	$30° \leq \alpha \leq 90°$	Flow visualizations
Jiang *et al.*[7]	$100 \leq Re \leq 500$	$\alpha = 90°$ + vertical extension	DNS
Jiang *et al.*[11]	$Re = 3900$	$\alpha = 90°$ + vertical extension	DNS

Previous experimental visualizations have allowed an analysis of the wake evolution, which is however limited to a few characteristic features of the flow. The present paper exploits stereo-particle image velocimetry (stereo-PIV) measurements that represent a step forward in the investigation of the wake behavior, allowing a quantitative investigation through the extraction of velocity distribution in specific regions of the flow domain. These data could be used as a reference for future numerical simulations.

The paper aims at presenting a comprehensive investigation of the flow features by analyzing both the mean velocity profiles, extracted along concentric arcs parallel to the cylinder axis, and the velocity modes obtained from spectral proper orthogonal decomposition of the measured PIV velocity. A schematic of the flow field topology results from both these analyses. The first part of the paper is devoted to the analysis of a quarter-of-ring configuration to clarify the disagreement between numerical and experimental results (which we ascribe to the treatment of free-end conditions) by examining the topology and the wake dynamics at various Reynolds numbers. The study is completed with an investigation of the influence of curvature, considering cylinders with the same arc length.

II. METHODOLOGY

A. Experimental set-up

The experimental measurements were carried out in a closed-loop free-surface water channel manufactured by Rolling Hills Research Corporation, with an average turbulence intensity over the tested velocity range less than 2%, in which constant curvature cylinders are immersed. The test section is $L_x = 1.52$ m long, $L_y = 0.38$ m wide, and $L_z = 0.51$ m deep; the cylinders are positioned such that their root is located above the water-free surface and they are immersed in the water channel with the free-end pointing toward the channel bottom. A sketch of the positioning of the cylinder within the water channel is shown in Fig. 2 for the $\alpha = 90°$ configuration.

The cylinders are placed in the center of the tunnel, and the flow direction is from the left to the right. Various Reynolds numbers and angles of curvature have been studied, whose values are reported in Table II. The configuration for the lowest ($\alpha = 45°$) and the highest ($\alpha = 90°$) curvatures is shown, respectively, in the left and right panels of Fig. 1. The curved cylinders were mounted to a rig overhead via a shaft coupler; they were realized by directly bending anodized aluminum rods, with a maximum curvature error of 1% (the estimated deflection is on the order of 100 μm).

The velocity flow field was measured by means of stereo-PIV technique. We generated a laser sheet (coming from the tunnel bottom) using a Nd:YAG laser (Litron Bernoulli PIV 100–25) to illuminate the lee-side wake of the cylinder. The sheet is stereoscopically imaged from the same side of the water channel with two hybrid CCD/CMOS cameras equipped with Scheimpflug lens adapters (LaVision, Imager sCMOS). The laser and the camera are synchronized with a programmable timing unit; their mutual position is shown in Fig. 2. 720 image pairs with a delay of 2400–8000 μs between exposures depending on the Reynolds number are acquired, at an overall sampling frequency of 24 Hz. For the seeding, hollow glass spheres having an average diameter of 10 μm and a specific gravity of 1.05 are used.

After calibration to a stereoscopic target, the dewarped images are $2607 \times 2181\,\text{pixels}^2$ resolution where the cylinder diameter is

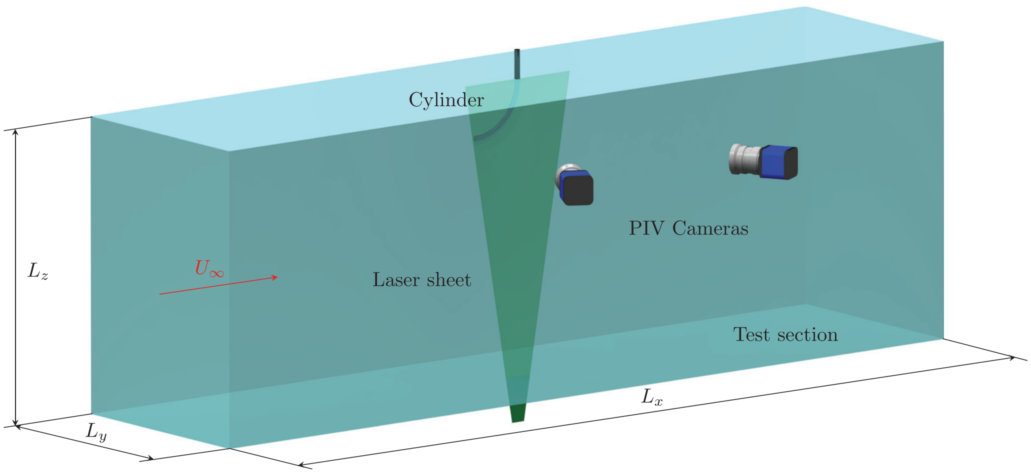

FIG. 2. Schematic of the experimental layout.

approximately 52 pixels. PIV velocity fields are computed with a spatial cross-correlation algorithm using LaVision DaVis 10.0 software. The data are processed using six passes with 50% overlap: two passes with a 128×128 pixels^2 interrogation window, two passes with a 64×64 pixels^2 window, and two passes with a 32×32 pixels^2 window. This results in velocity fields with a resolution of 163×138 vectors. The velocity fields are then post-processed using an anisotropic de-noising scheme with a 5×5 vector kernel and 2nd-order polynomial fit.

B. SPOD data reduction

The wake dynamics was investigated by means of SPOD technique, which provides the spatial and temporal evolution of coherent structures through the decomposition of the flow in various modes, ordered (for each frequency) by their energy content. A brief recall of this technique is presented hereafter.

Following the works of Towne *et al.*[20] and Schmidt *et al.*,[21] considering a zero-mean field $\boldsymbol{q}(\boldsymbol{x}, t)$, where $\boldsymbol{x}$ and t stand, respectively, for the spatial coordinates vector and the time, the snapshots ensemble $\{\boldsymbol{q}_i\}$ is organized to form a data matrix $\boldsymbol{Q}$ and then divided into N_b blocks, even overlapping each other. For each Nth block, a Fourier transform is computed, usually based on the Welch periodogram method. The Fourier component realizations are reordered by frequency, forming the matrix $\hat{\mathbf{Q}}_{f_k}$ for each frequency f_k, and then, a standard POD is performed on these matrices, namely, an eigenvalue/eigenvector problem for the cross-spectral correlation matrix

$$\mathbf{S}_{f_k} = \hat{\mathbf{Q}}_{f_k} \hat{\mathbf{Q}}'_{f_k} \tag{1}$$

in which the asterisk represents the conjugate transpose. With a such decomposition, SPOD modes ($\boldsymbol{\Phi}_{f_k}$) and eigenvalues ($\boldsymbol{\Lambda}_{f_k}$) are computed solving

$$\mathbf{S}_{f_k} \boldsymbol{W} \boldsymbol{\Phi}_{f_k} = \boldsymbol{\Phi}_{f_k} \boldsymbol{\Lambda}_{f_k}, \tag{2}$$

obtained for each frequency, being $\boldsymbol{W}$ a spatial weight matrix taking into account the non-uniformity of the data. The problem (2) is frequently replaced by the smaller eigenvalue problem (snapshots method)

$$\hat{\mathbf{Q}}^*_{f_k} \boldsymbol{W} \hat{\mathbf{Q}}_{f_k} \boldsymbol{\Psi}_{f_k} = \boldsymbol{\Psi}_{f_k} \tilde{\boldsymbol{\Lambda}}_{f_k}, \tag{3}$$

where $\tilde{\boldsymbol{\Lambda}}_{f_k}$ are the non-zero eigenvalues of (2), while the eigenvectors are $\boldsymbol{\Phi}_{f_k} = \hat{\mathbf{Q}}_{f_k} \boldsymbol{\Psi}_{f_k}$.

TABLE II. Experiments test matrix of the studied cases.

L/D	D	Re	α (deg)			
30	4.8 mm	240–880	45	60	75	90

Once the SPOD modes have been identified, a low-rank reconstruction of the field can be performed either in frequency or in the temporal domain, as shown by Nekkanti and Schmidt.[22]

Here, the field $\boldsymbol{q}$ contains the fluctuating velocity components u, v, and w, and the weight matrix $\boldsymbol{W}$ has been chosen such that the inner product is proportional to the integral of the turbulent kinetic energy[23]

$$\boldsymbol{q} = \begin{bmatrix} u \\ v \\ w \end{bmatrix}, \quad \boldsymbol{W} = \int_V \begin{bmatrix} 1 & & \\ & 1 & \\ & & 1 \end{bmatrix} dV;$$

note that a zero weight has been assigned to the portion of fluid upstream of the cylinder.

The SPOD analysis was carried out partitioning the $N = 720$ digital images in $N_b = 10$ blocks containing $N_f = 128$ snapshots each; a 50% overlap was applied between the block, reducing the spectral leakages with a standard Hamming window.

III. RESULTS

A. A quarter-of-ring curved cylinder

We first discuss the flow behind a quarter-of-ring curved cylinder ($\alpha = 90°$) at Re $=240$.

1. The flow topology

The analysis of the wake evolution behind a curved cylinder consists in the extraction of velocity profiles along concentric arcs parallel to the cylinder axis.[7,8] In the present paper, we selected a concentric arc located at 1.5 diameters from the leeward face of the cylinder (hereafter referred to as 1.5D arc). In Fig. 3, we report the mean velocity projected along the cylinder axis (mean axial velocity V_{ax}, solid red line), together with the mean stream-wise ($\bar{u}$, dashed blue line) and the cross-wise ($\bar{w}$, dot-dashed black line) velocity profiles along the 1.5D arc. The uncertainty shown is the standard deviation of independent snapshot measurements, with a maximum value of 4.2%. All velocities are made non-dimensional by the free-stream velocity U_∞ and are reported as a function of the non-dimensional curvilinear abscissa $s^* = s/D$ (bottom axis) and of the angular position θ (top axis). In Fig. 4, we show the snapshot of the instantaneous span-wise velocity component (v/U_∞), where the red solid and the black dashed line indicate, respectively, the cylinder leeward side and the arc along which the axial velocity is extracted. Note that the flow field upstream of the cylinder has not been measured, thus appearing as a uniform zero region in the figure.

For $s^* \leq 5$ ($\theta \leq 15°$), the mean axial velocity is approximately equal to the free-stream velocity, an indication that the flow is not altered by the presence of the cylinder at a distance 1.5D from the wall. As s^* increases, V_{ax} decreases mainly because of the cylinder shelter effect, attaining a minimum at $s^* = 10$. The wake in this region is dominated by two counter-rotating stationary vortices that do not affect the span-wise velocity distribution in the x–z plane. Secondary structures are observed close to the cylinder surface. The action of the vortex pair is to induce a velocity toward the cylinder root, and so to increase the velocity cross-wise component. Simultaneously, the stream-wise velocity component exhibits a continuous decrease. This action extends up to $s^* = 19$ ($\theta = 57°$) where $\bar{w}$ attains a maximum. The standing stationary vortices then evolve into an oblique shedding regime past $s^* = 19$ (the angular location where this occurs is highlighted by the dot-dashed line in Fig. 4), and the mean cross-wise velocity component undergoes a continuous decrease. Note that the numerical simulations by Jiang *et al.*[7] show that for a concave cylinder with a straight vertical extension protruding from the cylinder edge, the shedding occurs at the location where the mean stream-wise velocity becomes negative. Furthermore, moving along the arc, both velocity components tend to zero.

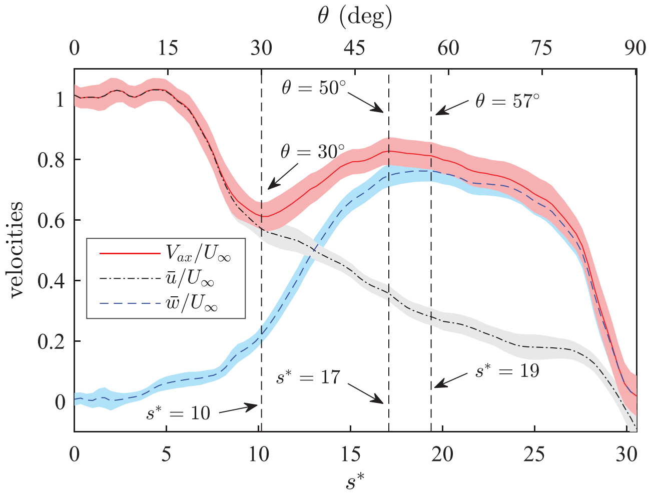

FIG. 3. Distributions of the mean axial (V_{ax}/U_∞), stream-wise ($\bar{u}/U_\infty$), and cross-wise ($\bar{w}/U_\infty$) velocities along a concentric arc located 1.5D from the leeward face of the cylinder. $\alpha = 90°$ and $Re = 240$. The uncertainty shown is the standard deviation of independent snapshot measurements.

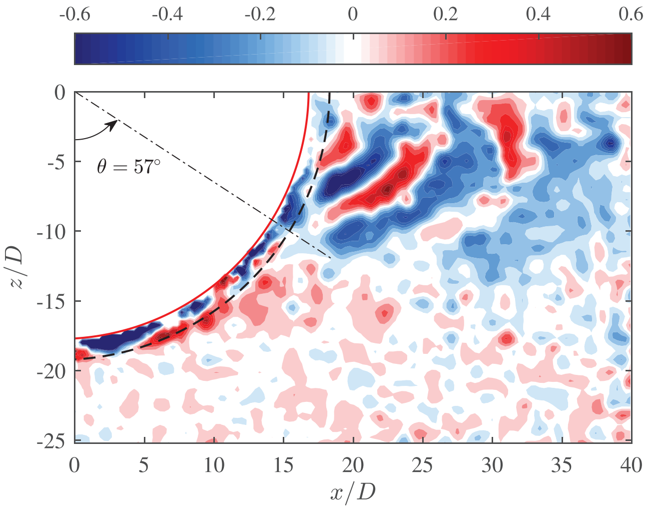

FIG. 4. Snapshot of the instantaneous span-wise velocity component (v/U_∞) for the case $\alpha = 90°$ at $Re = 240$. The red solid line represents the end of the cylinder leeward face, and the black dashed line identifies the arc at 1.5D.

The observed oblique shedding pattern extends for approximately 15 diameters downstream of the cylinder lee-side up to the free surface. This regime is mainly related to the finite of the upwash cross-wise velocity (note from Fig. 3 that $\bar{w}/U_\infty \geq 0.6$ till $\theta \approx 80°$), which causes vortices to roll up at an angle to the cylinder.[6]

2. The wake transition

The wake dynamics and its structures are strongly affected by the Reynolds number. The wake becomes more and more irregular when *Re* increases with the appearance of fine-scale structures on the primary vortex (typical of type-A and type-B instabilities) and of regions of vortex dislocation.

To investigate the wake transition, we scrutinize the velocity distributions at various Reynolds numbers, in the range between $Re = 240$ (the reference case) and 840 with a step $\Delta Re = 120$. The distributions of the axial, and the stream- and cross-wise velocities are reported, respectively, in Figs. 5 and 6. The contour of the stream-wise velocity component is reported in Fig. 7 at various *Re*.

The axial velocity remains unchanged ($V_{ax}/U_\infty \approx 1$) for all *Re* numbers for $s^* \leq 5$; then, different behaviors are observed. In agreement with the findings of Jiang *et al.*,[7] as the Reynolds number increases the location where V_{ax} attains its minimum moves toward the free-end of the cylinder, due to a sudden recovery of the $\bar{u}$ velocity component that produces a shift of the location of the minimum to $s^* \approx 7$. As observed above, the minimum of V_{ax} results from the combined effects of the decrease in $\bar{u}$ (due to the cylinder shelter effect) and the increase in $\bar{w}$ that is associated with the velocity induced by the counter-rotating stationary vortices. When *Re* increases, the zone where $\bar{u}$ is reduced shrinks and is confined behind the cylinder in the region between the cylinder surface and the 1.5D arc (Fig. 7). Moreover, at the same time, for increasing values of *Re*, a tip vortex

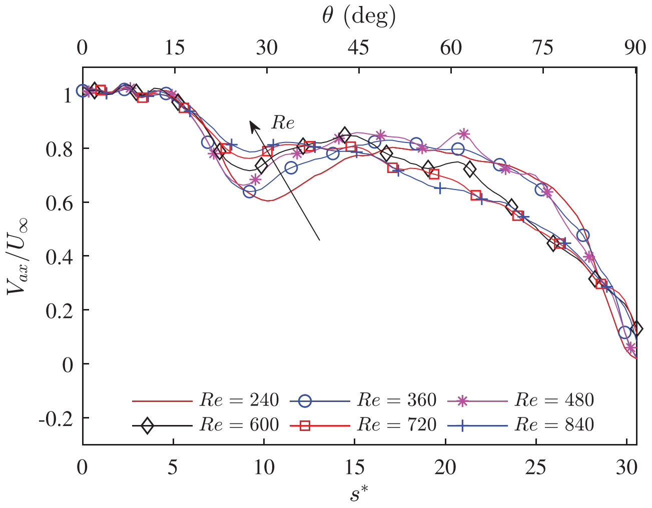

FIG. 5. Distribution of the mean axial velocity (V_{ax}/U_∞) along the 1.5D arc at various *Re* numbers. $\alpha = 90°$.

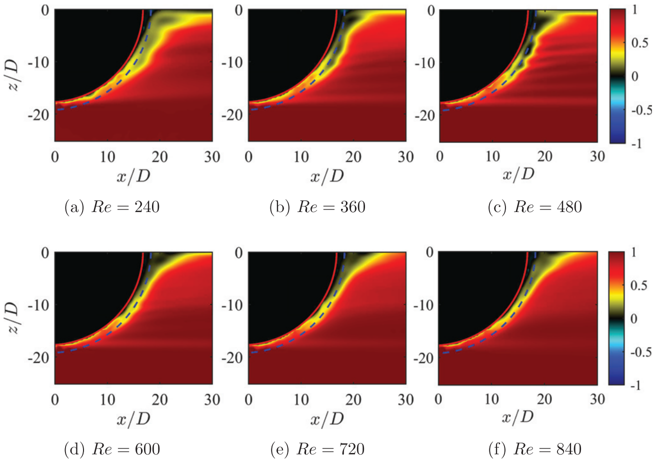

(a) $Re = 240$ (b) $Re = 360$ (c) $Re = 480$

(d) $Re = 600$ (e) $Re = 720$ (f) $Re = 840$

FIG. 7. Map of the mean stream-wise velocity ($\bar{u}/U_\infty$) at various *Re* numbers.

appears at the free-end of the cylinder, causing a local reduction of the stream-wise velocity (see Fig. 6, right panel). This effect is maximum at $Re = 480$ and reduces for higher *Re*. In conclusion, at low *Re*, moving along the 1.5D arc, the stream-wise velocity constantly reduces and the effect of the tip vortex is nearly negligible, whereas, when *Re* increases, the initial reduction of $\bar{u}$ due to the presence of this vortex is followed by a sudden recovery, exiting the vortex, and then, it continues to decrease. At $Re = 840$, the velocity local minima (both in $\bar{u}$ and V_{ax}) are barely appreciable. The variation with the Reynolds number of the position where the stream-wise velocity attains a local minimum gives a quantitative information of the dependency of the tip vortex on *Re*. The results show that the position where the minimum is found varies between $\theta = 27°$ and $29°$. This indicates that the tip vortex formed at the free-edge is slightly tilted toward the root of the cylinder. Indeed, from geometrical considerations, if the tip vortex axis were parallel to the velocity-free stream direction, it would the 1.5D arc at $\theta = 25°$. It is important to observe that for all Reynolds numbers, the $\bar{w}$ velocity profiles are not affected by the tip vortex. Note that the presence of the latter was already observed by Shang *et al.*;[6] however, its effects were not quantified.

Downstream of $s^* \approx 14$ ($\theta \approx 40°$), the main contribution to the axial velocity is due to the cross-wise velocity component, whose evolution is strongly affected by the Reynolds number. When *Re* increases, the wake exhibits a more irregular nature and the shedding zone presents a greater extension. As a consequence, the effects of the standing counter-rotating vortices are limited to a narrow region along the cylinder free-end, and consequently, the cross-wise velocity maximum is displaced, moving from $s^* = 19$ ($\theta = 57°$) at $Re = 280$ to $s^* = 15$ ($\theta = 45°$) at $Re = 840$. It is also interesting to observe that when varying *Re*, the $\bar{w}$ velocity component (for $14 \le s^* \le 27$) first increases up to $Re \le 480$; then, it starts to decrease reaching a minimum at $Re = 840$. At the same time, the velocity profile loses its bell-

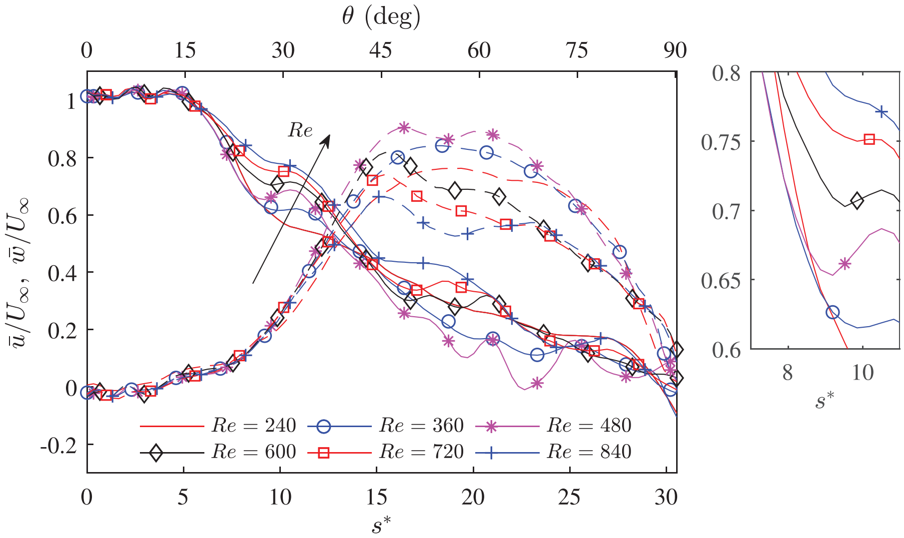

FIG. 6. Distributions of the mean stream-wise ($\bar{u}/U_\infty$, solid lines) and cross-wise ($\bar{w}/U_\infty$, dashed lines) velocities along the 1.5D arc at various *Re* numbers (left panel). Zoom of the mean stream-wise velocity distribution (right panel). $\alpha = 90°$.

shaped character. This variation is ascribed to the laminar–turbulent wake transition in agreement with the findings of Shang *et al.*[6] and Jiang *et al.*[7] The axial velocity (and the transition process) directly affects the flow topology and the shedding angle. As previously observed the upwash velocity is responsible for the roll up of the vortices at an angle to the cylinder, the inclination of the vortex shedding follows the same trends of the cross-wise velocity, attaining a maximum at $Re \approx 480$. Then, it tends to align with the cylinder axis. The change in the inclination goes along with variations in the wake topology and its dynamics (i.e., vortex dimensions and shedding frequencies), as discussed in the next Sec. III A 3.

3. The wake dynamics

The dynamics of the wake are investigated by analyzing the spatial and temporal characteristics of the SPOD modes. Figure 8 reports the spectrum at the reference Reynolds number ($Re = 240$). In the figure, the normalized SPOD eigenvalues (for each mode of the span-wise velocity component) are presented as a function of the Strouhal number $St = fD/U_\infty$. The region of interest is the one in which the spectrum shows a clear separation between the first and the other modes. This zone is in the range of $0.035 \le St \le 0.155$ ($0.185 \le f \le 1.7$) and is peaked at $St = 0.085$ ($f = 0.94$ Hz), which represents the maximum separation point between the first two SPOD modes.

The real and imaginary parts of the first SPOD mode at the leading frequency are reported, respectively, in the left and right panel of Fig. 9. They both exhibit an oblique pattern that reproduces the shedding mode behind the cylinder.[12] The distinguishing features of the flow (inclination and spatial wavelength of the vortex shed from the separation line along the cylinder lee-side, Shang *et al.*[6]) are well identified, corroborating the previous analysis based on scrutiny of the velocity distributions. It is interesting to note that the real and the imaginary parts are not in phase, due to the traveling nature of the motion, an indication of shedding structures advected downstream.

The SPOD confirms the establishment of the oblique shedding for $z/D < -12$ and $\theta \approx 57°$ that extends in the stream-wise direction throughout the domain (Fig. 4). The SPOD structures being representative of the turbulent kinetic energy of the flow, one may conclude that, moving in the stream-wise direction, the vortex shedding loses its coherence still maintaining its kinetic energy content.

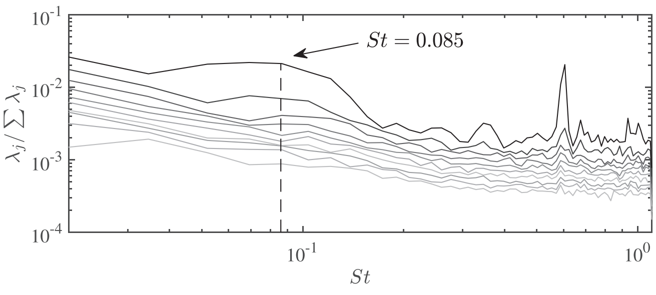

FIG. 8. SPOD spectrum for $\alpha = 90°$ configuration at $Re = 240$.

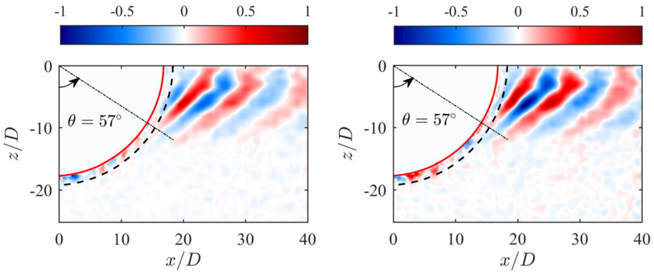

(a) Real part.

(b) Imaginary part.

FIG. 9. Map of the first SPOD mode of the span-wise velocity (v) at $St = 0.085$. Real part, panel (a), and imaginary part, panels (b).

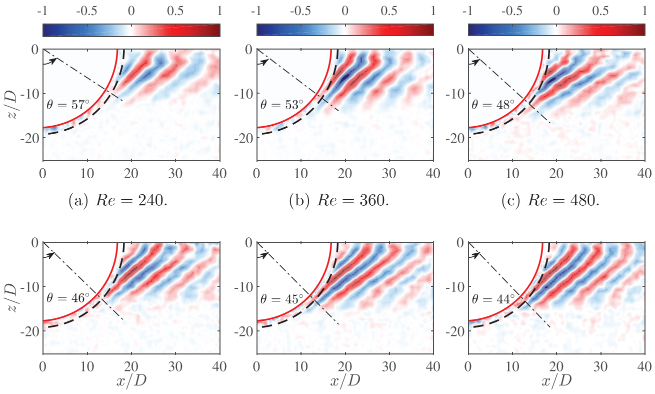

(a) $Re = 240$.

(b) $Re = 360$.

(c) $Re = 480$.

(d) $Re = 600$.

(e) $Re = 720$.

(f) $Re = 840$.

FIG. 10. Map of the first SPOD mode of the span-wise velocity (v) at $\alpha = 90°$ for various *Re*. The dash-dotted line identifies the onset location of the oblique shedding.

Figure 10 reports the first SPOD modes at the leading frequency at various *Re*. The figure shows that as the Reynolds number increases, the onset of the oblique vortex shedding moves continuously from $\theta = 57°$ (at $Re = 240$) to $\theta = 44°$ (at $Re = 840$). As for the vortex inclination, it exhibits a different trend. It first increases with Re varying from $\varphi = 48°$ (at $Re = 480$) to $\varphi = 59°$ (at $Re = 480$). Then, increasing the Reynolds number, the transition to turbulence is triggered with a consequent increase in the shedding frequency and a decrease in the wavelength, and the vortex inclination decreases reaching a value of $\varphi = 49.5°$ at $Re = 840$. The values of the peak Strouhal number, the angular position of the onset of the vortex shedding, and its inclination angle (St, θ, and φ) at various *Re* are summarized in Table III.

B. Generic concave curved cylinder

Previous studies[6,12] showed that curvature has a major effect on the topology and the evolution of the wake behind curved cylinders,

TABLE III. Wake properties at various *Re*.

Re	240	360	480	600	720	840
St	0.087	0.106	0.089	0.114	0.113	0.122
$\theta°$	57°	53°	48°	46°	45°	44°
$\varphi°$	48°	49°	59°	51°	51°	49.5°

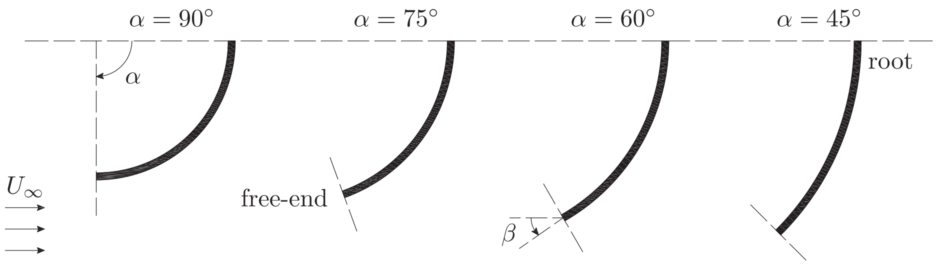

FIG. 11. Sketch of the concave curved cylinders at different curvatures.

highlighting that the transition Reynolds number from laminar to turbulent regime increases with curvature. Here, we analyze the combined effects of the curvature and the Reynolds number considering four different values of α (the lower the α the lower the curvature, see Fig. 11). Note that the length of the cylinder is the same for all curvatures, with s^* spanning between 0 (the free-end) and 30 (the root of the cylinder).

As α reduces, the angle between the free-stream velocity and the cylinder axis (β) at the free-end increases (see Fig. 11), and the tip-vortex that results from the rapid acceleration experienced near the free-end strengthen. Figure 12 shows indeed that for decreasing α V_{ax}/U_∞ attains values greater than unity at $s^* = 0$; then, it drops rapidly moving away from the cylinder tip. The axial velocity also exhibits a minimum that moves toward decreasing s^* as the curvature decreases ($s^*_{\min} = 4.2$, 2.2, 1.8 for $\alpha = 75°$, 60°, 45°, respectively). It then experiences a short recovery moving out of the tip vortex followed by a reduction due to the cylinder shelter effect. Similar behavior is observed in the stream-wise velocity distribution reported in Fig. 13. On the contrary, the cross-wise velocity component increases at a rate nearly unaffected by the curvature as the standing stationary vortices merge into the oblique vortices whose onset is almost unaffected by the curvature (s^* of onset equal to 19 and 21, and approximately 17 for $\alpha = 75°$, 60°, and 45°, respectively). It is interesting to observe that for $\alpha = 45°$, the onset of the oblique shedding regime does not occur where the mean cross-wise velocity component peaks, but, due to the strengthening of the counter-rotating vortex pair associated with secondary vortical structures forming at the sides of the free-end surface, it occurs at $s^* = 17$.

The topology of the flow is represented in Fig. 14 in terms of the real part of the first SPOD mode of the span-wise velocity at the leading frequency. The figure shows that all configurations exhibit oblique shedding in the central part of the cylinder lee-side. Close to the root the shedding becomes nearly normal to the cylinder axis. The figure also confirms that the vortex inclination is weakly affected by the curvature (ϕ varying between 43° and 44°, for α in the range $75° - 45°$).

The wavelength of the vortex shedding decreases with as the curvature is reduced in agreement with the findings of Shang *et al.*,[6] who showed that the transition to turbulence occurs at lower Reynolds numbers and that turbulent regimes exhibit smaller wavelengths (at lower curvatures).

1. The $\alpha = 45°$ configuration

In this section, we discuss the influence of the Reynolds number on the $\alpha = 45°$ configuration that was previously shown to be the most affected by the free-end effects. For the analysis, the Reynolds number is varied in the range of 240 and 840 as for the $\alpha = 90°$ configuration. We focus on the mean stream-wise and cross-wise velocity components whose distributions along 1.5D arc are reported, respectively, in Figs. 15 and 16 at various *Re*. As for the topology, in Fig. 17, the real part of the first SPOD modes of the span-wise velocity component at the leading frequency at various *Re* is reported.

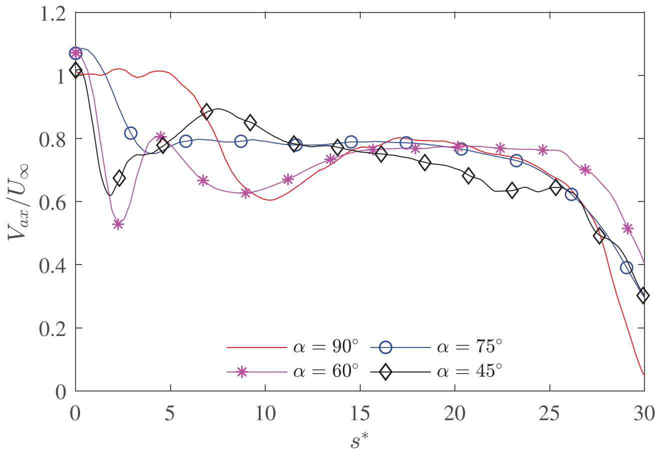

FIG. 12. Distributions of the mean axial velocity (V_{ax}/U_∞) along the 1.5D arc at various curvatures at $Re = 240$.

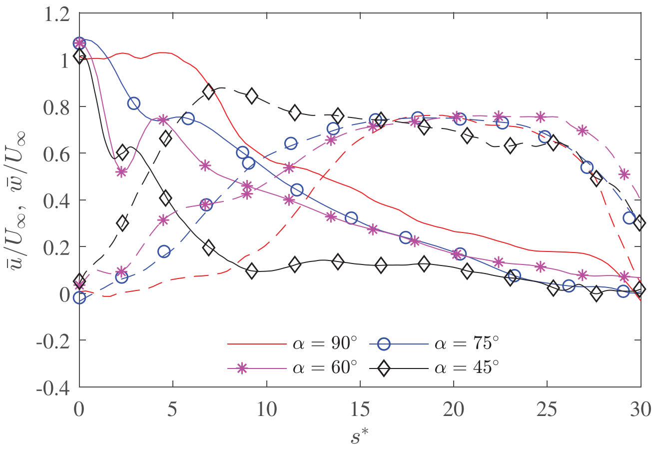

FIG. 13. Distributions of the mean stream-wise ($\bar{u}/U_\infty$, solid lines) and cross-wise ($\bar{w}/U_\infty$, dashed lines) velocities along the 1.5D arc at various curvatures at $Re = 240$.

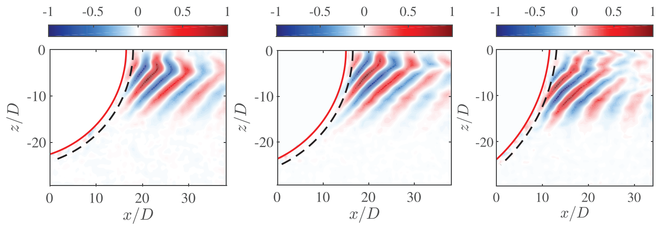

(a) $\alpha = 75°$. (b) $\alpha = 60°$. (c) $\alpha = 45°$.

FIG. 14. Map of the first SPOD mode of the span-wise velocity component (v) at various curvatures at $Re = 240$.

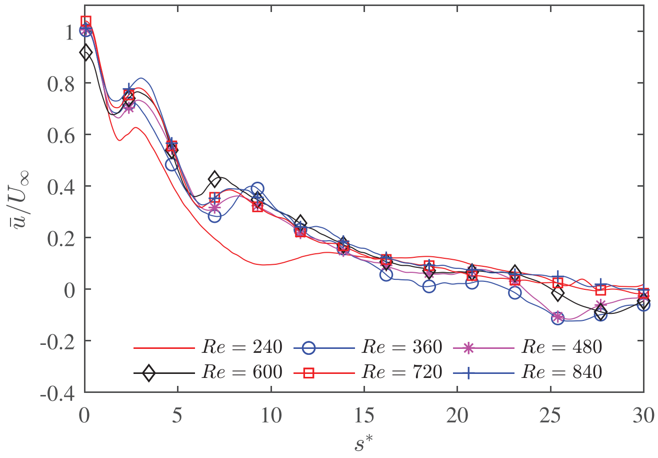

FIG. 15. Distribution of the mean stream-wise ($\bar{u}/U_\infty$) velocity along the 1.5D arc at various Re for $\alpha = 45°$.

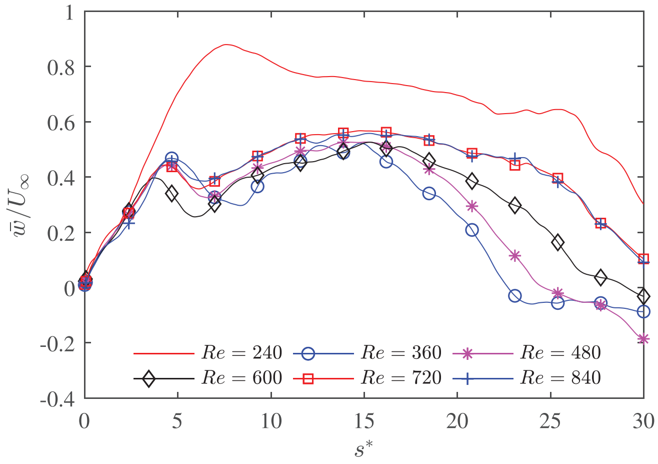

FIG. 16. Distribution of the mean cross-wise ($\bar{w}/U_\infty$) velocity along the 1.5D arc at various Re for $\alpha = 45°$.

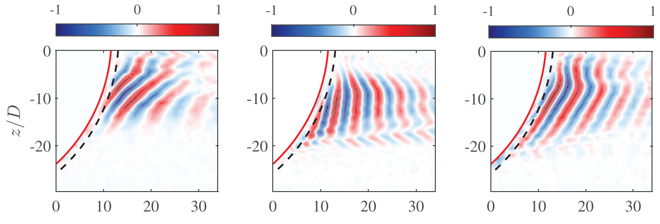

(a) $Re = 240$. (b) $Re = 360$. (c) $Re = 480$.

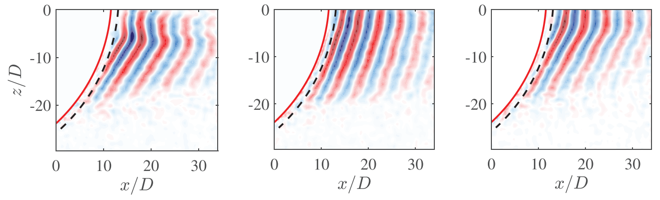

(d) $Re = 600$. (e) $Re = 720$. (f) $Re = 840$.

FIG. 17. Map of the first SPOD mode of the span-wise velocity (v) at $\alpha = 45°$ for various Re.

For $Re = 240$, the flow is laminar and the onset of shedding occurs past the local cross-wise mean velocity peak. As Re increases, the wake becomes irregular, the flow transitions to turbulent and both the stream-wise and cross-wise mean velocity components exhibit reduced oscillations. Transition starts at $Re = 360$ ($s^* \approx 9$), with structures almost aligned with the cylinder axis [$\phi \approx 11°$, see Fig. 17 panel (b)]. Moving along the concentric arc, for $Re = 360$, one first observes a local reduction of $\bar{u}$ due to the presence of the tip vortex. Then, the wake is dominated by the standing vortex pair that makes the cross-wise velocity to increase attaining a peak at $s^* = 4.7$. The action of these vortices is limited to the near-cylinder surface. Unlike the quarter-of-ring case, where they interact with the shedding (see the work by Ref. 7), these vortices stretch in the stream-wise direction inducing a local minimum around $s^* \approx 7$ (both in the $\bar{u}$ and $\bar{w}$ velocity distributions) where the onset of the shedding regime occurs. As higher Reynolds numbers, a similar trend is observed. The flow is fully turbulent, the mean stream-wise velocity component is rather independent of Re for $s^* \leq 22$ (Fig. 15), whereas $\bar{w}$ exhibits a weak dependence on Re for $s^* \leq 15$ (Fig. 16). In the range of Re here analyzed, we can conclude that the onset of the shedding regime and the effects of the standing vortices are slightly influenced by the Reynolds number.

2. Flow topology

Based on the analyses of the velocity distributions and of the SPOD structures, this section aims at presenting a schematic of the flow field (topology, wake regime, effects of the curvature, and the Reynolds number) behind curved cylinders with a free-end.

Figure 18 reports the location of the onset of the shedding associated with different Reynolds numbers. As Re increases, the shedding region expands moving toward the cylinder free-end attaining an asymptotic position (s_a^*) that depends on α. A reduction of the curvature tends to favor transition and consequently s_a^* reduces from a value $s_a^* = 19$ (at $\alpha = 90°$ and $Re = 840$) to $s_a^* = 7.5$ (at $\alpha = 45°$ and $Re = 360$).

Figure 19 shows the leading Strouhal number of the first SPOD mode as a function of the Reynolds number. The $\alpha = 90°$ case exhibits a drop at $Re = 480$ with a consequent transition to turbulence due to type-A instability.[9,12] For the $\alpha = 45°$ configuration that transitions between $Re = 240$ and 360, the Strouhal number exhibits a drop at $Re = 480$. In accordance with Williamson,[10] this drop identifies the

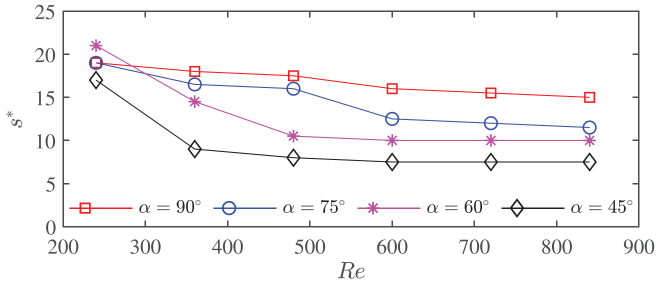

FIG. 18. Onset location of the shedding regime as a function of the Reynolds numbers.

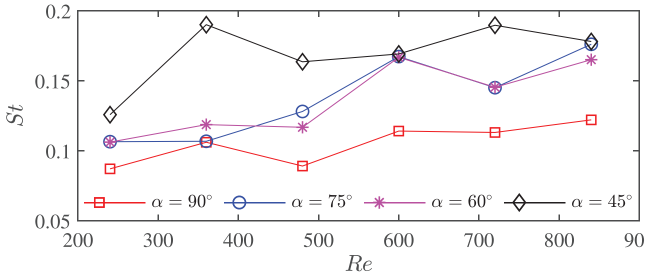

FIG. 19. Leading Strouhal numbers of the first SPOD mode as a function of the Reynolds numbers.

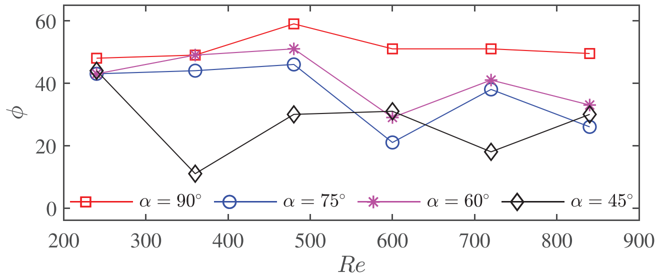

FIG. 20. Local vortex inclination as a function of the Reynolds numbers.

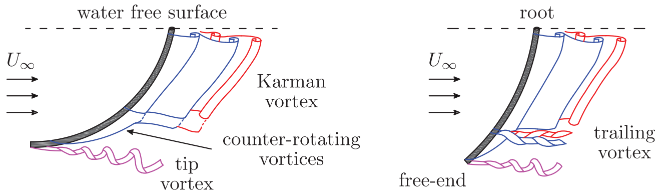

FIG. 21. Schematic of the flow field topology behind a curved concave cylinder. Left panel refers to a quarter-of-ring case, $\alpha = 90°$; the right panel depicts the $\alpha = 45°$ configuration.

vortex dislocation. By the previous analysis, the $\alpha = 75°$ and $\alpha = 60°$ configurations should experience a type-A instability, with a subsequent transition to turbulence, at a Reynolds number in the range bounded by the transition Reynolds number of $\alpha = 45°$ and the one of the $\alpha = 90°$. Therefore, the drop in the Strouhal number at $Re = 720$ identifies the vortex dislocation.

The local vortex inclination, ϕ, reported in Fig. 20 does not show a clear trend. From the figure, one observes that the vortex inclination reduces around transition, and then, it increases as the regime changes into turbulent.

A schematic of the flow topology is reported in Fig. 21 for the configurations $\alpha = 90°$ (left panel) and $\alpha = 45°$ (right panel). The oblique vortex shedding is associated with the formation of von Karman vortex sheets (VKVS) that interact with the standing counter-rotating vortices. As shown in Fig. 6 for $\alpha = 90°$, the cross-wise velocity exhibits a bell-shaped distribution whose peak along the 1.5D arc corresponds to the onset of the shedding, location where the standing vortices are entrained by the forming VKVS. For $\alpha = 45°$, the cross-wise velocity distribution loses its bell-shaped form taking on a double-peak shape (Fig. 16) with a minimum corresponding to the trailing vortices, sketches in Fig. 21, stemming from the wall.

We note that these flow features are not always observed in previous experiments and simulations. For example, for the $\alpha = 90°$, the vortex shedding is not observed neither in the DNS simulations of Jiang *et al.*[7] (we argued because of the imposed boundary conditions), neither in the first experimental campaign by Shang *et al.*[6] Furthermore, high-resolution experimental measurements and high-fidelity numerical simulations are required to clarify on the one hand the flow features around the free-edge, and on the other the interaction between the counter-rotating vortices pair and the von Karman vortex sheets.

IV. CONCLUSIONS

The investigation of the wake flow behind concave curved cylinders has been experimentally carried out by means of stereo-PIV velocity measurements in the cylinder plane of curvature. For the analysis, we have scrutinized the mean velocity components extracted along concentric arcs parallel to the leeward side of the cylinder. The spectral proper orthogonal decomposition of the instantaneous velocity field has been used to characterize the dynamics of the most relevant flow structures at various Reynolds numbers and curvature.

Compared with previous works, these experimental measurements have allowed us to provide further details on the features of the flow field. It is first shown that the flow behind a quarter-of-ring cylinder presents a topology dominated by an oblique vortex shedding in the upper part (close to the cylinder root), differently from what is observed in similar literature cases. This difference has been attributed to the treatment of the role of the free-end that triggers the wake toward a shedding regime. The SPOD analysis has allowed to characterize the extension, the frequency of the shedding regime, and the local vortex inclination. The lower part of the domain (near the free-end), instead, presents two counter-rotating standing stationary vortices that induce an upward cross-wise velocity, and (at the free-end) a tip vortex that tilts upward and expands as it evolves downstream. The boundary "separating" the stationary regime from shedding one is determined by maximum of the cross-wise velocity.

Increasing the Reynolds number, the shedding zone presents a greater extension (expanding toward the cylinder free-end), and the wake is more irregular in nature with fine-scale structures on the von Karman vortex sheet. The shedding frequency, generally, increases and exhibits local drops due to the onset of vortex instabilities and the appearance of the vortex dislocation. The inclination of the shedding, instead, is strictly related to the Reynolds number. Laminar regimes show an increasing inclination with *Re*, whereas flow transition is accompanied by a reduction of the vortex inclination, which then increases as the flow becomes turbulent.

A decrease in curvature increases the effect of the free-end, with a consequent strengthening of the tip-vortex. The standing vortices that develop on the leeward side along the cylinder surface are entrained and merge with the forming von Karman vortex sheets. For the least curved configuration, the standing vortices stretch in the stream-wise direction and lift off the cylinder surface, the cross-wise velocity distribution loses its bell-shaped form taking on a double-peak shape with a minimum corresponding to the trailing vortices stemming from the wall.

ACKNOWLEDGMENTS

The authors wish to thank Kai Kindred for his support during the experimental campaign. Matteo Chiatto acknowledges the support of the Fulbright fellowship at Princeton University. Jessica K. Shang and Caroline Cardinale were supported by the U.S. Office of Naval Research under Award No. N00014-18-1-2456. Francesco Grasso acknowledges Global Scholar research funds by Princeton University.

AUTHOR DECLARATIONS

Conflict of Interest

The authors have no conflicts to disclose.

Author Contributions

Matteo Chiatto: Writing – original draft (equal); Writing – review & editing (equal). **Caroline Cardinale:** Writing – review & editing (equal). **Jessica K. Shang:** Writing – review & editing (equal). **Francesco Grasso:** Writing – review & editing (equal).

DATA AVAILABILITY

The data that support the findings of this study are available from the corresponding author upon reasonable request.

REFERENCES

[1] A. Miliou, S. Sherwin, and J. Graham, "Fluid dynamic loading on curved riser pipes," J. Offshore Mech. Arct. Eng. **125**, 176–182 (2003).

[2] A. Miliou, A. De Vecchi, S. Sherwin, and J. Graham, "Wake dynamics of external flow past a curved circular cylinder with the free stream aligned with the plane of curvature," J. Fluid Mech. **592**, 89–115 (2007).

[3] A. de Vecchi, S. Sherwin, and J. Graham, "Wake dynamics of external flow past a curved circular cylinder with the free-stream aligned to the plane of curvature," J. Fluids Struct. **24**, 1262–1270 (2008).

[4] G. Assi, N. Srinil, C. Freire, and I. Korkischko, "Experimental investigation of the flow-induced vibration of a curved cylinder in convex and concave configurations," J. Fluids Struct. **44**, 52–66 (2014).

[5] J. Gallardo, H. Andersson, and B. Pettersen, "Turbulent wake behind a curved circular cylinder," J. Fluid Mech. **742**, 192–229 (2014).

[6] J. Shang, H. Stone, and A. Smits, "Flow past finite cylinders of constant curvature," J. Fluid Mech. **837**, 896–915 (2018).

[7] F. Jiang, B. Pettersen, H. Andersson, J. Kim, and S. Kim, "Wake behind a concave curved cylinder," Phys. Rev. Fluids **3**, 094804 (2018).

[8] F. Jiang, B. Pettersen, and H. Andersson, "Influences of upstream extensions on flow around a curved cylinder," Eur. J. Mech. B **67**, 79–86 (2018).

[9] C. Williamson, "Three-dimensional wake transition," J. Fluid Mech. **328**, 345–407 (1996).

[10] C. Williamson, "Oblique and parallel modes of vortex shedding in the wake of a circular cylinder at low Reynolds numbers," J. Fluid Mech. **206**, 579–627 (1989).

[11] F. Jiang, B. Pettersen, and H. Andersson, "Turbulent wake behind a concave curved cylinder," J. Fluid Mech. **878**, 663–699 (2019).

[12] M. Chiatto, J. Shang, L. De Luca, and F. Grasso, "Insights into low Reynolds flow past finite curved cylinders," Phys. Fluids **33**, 035150 (2021).

[13] S. Ramberg, "The effects of yaw and finite length upon the vortex wakes of stationary and vibrating circular cylinders," J. Fluid Mech. **128**, 81–107 (1983).

[14] A. Slaouti and J. Gerrard, "An experimental investigation of the end effects on the wake of a circular cylinder towed through water at low Reynolds numbers," J. Fluid Mech. **112**, 297–314 (1981).

[15] C. Park and S. Lee, "Effects of free-end corner shape on flow structure around a finite cylinder," J. Fluids Struct. **19**, 141–158 (2004).

[16] I. Afgan, C. Moulinec, R. Prosser, and D. Laurence, "Large eddy simulation of turbulent flow for wall mounted cantilever cylinders of aspect ratio 6 and 10," Int. J. Heat Fluid Flow **28**, 561–574 (2007).

[17] D. Sumner, "Flow above the free end of a surface-mounted finite-height circular cylinder: A review," J. Fluids Struct. **43**, 41–63 (2013).

[18] G. Hu, K. Tse, K. Kwok, and Y. Zhang, "Large eddy simulation of flow around an inclined finite square cylinder," J. Wind Eng. Ind. Aerodyn. **146**, 172–184 (2015).

[19] T. Kawamura, M. Hiwada, T. Hibino, T. Mabuchi, and M. Kumada, "Flow around a finite circular cylinder on a flat plate," Bull. JSME **27**, 2142–2150 (1984).

[20] A. Towne, O. Schmidt, and T. Colonius, "Spectral proper orthogonal decomposition and its relationship to dynamic mode decomposition and resolvent analysis," J. Fluid Mech. **847**, 821–867 (2018).

[21] O. Schmidt, A. Towne, G. Rigas, T. Colonius, and G. Bres, "Spectral analysis of jet turbulence," J. Fluid Mech. **855**, 953–982 (2018).

[22] A. Nekkanti and O. T. Schmidt, "Frequency-time analysis, low-rank reconstruction and denoising of turbulent flows using SPOD," J. Fluid Mech. **926**, A26 (2021).

[23] O. Schmidt and T. Colonius, "Guide to spectral proper orthogonal decomposition," AIAA J. **58**, 1023–1033 (2020).